Journal of Computational Physics **171,** 201–226 (2001)
doi:10.1006/jcph.2001.6783, available online at http://www.idealibrary.com on IDEAL®

The Quasilinear Wave Equation for Antiplane Shearing of Nonlinearly Elastic Bodies

Dawn A. Lott,* Stuart S. Antman,† and William G. Szymczak‡

*Center for Applied Mathematics and Statistics, Department of Mathematical Sciences, New Jersey Institute of Technology, Newark, New Jersey 07102; †Department of Mathematics, Institute for Physical Science and Technology, Institute for Systems Research, University of Maryland, College Park, Maryland 20742; and ‡Physical Acoustics Branch, Code 7131, Naval Research Laboratory, Washington, DC 20375
E-mail: dalc@dalc.njit.edu; ssa@math.umd.edu; szymczak@eeyore.nrl.navy.mil

Received November 30, 1999; revised March 5, 2001

We formulate an efficient numerical algorithm based on finite-difference approximations and inspired by algorithms from gas dynamics to treat the quasilinear wave equation

$$w_{tt} = \left[\alpha\left(w_x^2 + w_y^2\right) w_x\right]_x + \left[\alpha\left(w_x^2 + w_y^2\right) w_y\right]_y$$

governing antiplane motions of incompressible, isotropic nonlinearly elastic bodies in two-dimensions. In particular, we are concerned with the treatment of focusing and shocks for bodies whose material response differs markedly from that of linear elasticity. We carefully validate our method by comparing our results with those of the axisymmetric version of this equation in polar coordinates. © 2001 Academic Press

Key Words: nonlinear elasticity; antiplane motions; finite-difference methods; polar singularities.

---

1. INTRODUCTION

In this paper, we present effective numerical methods to treat focusing and shocks for quasilinear wave equations governing antiplane motions of nonlinearly elastic bodies in two-dimensional domains. Our problem, posed as a hyperbolic system of conservation laws, is treated by a second-order Godunov-type scheme that uses a conservative finite-difference update and the approximate Riemann solver of Davis [12].

In his important papers [32, 33], Trangenstein extended to problems of solid mechanics with several space dimensions the adaptive higher order Godunov schemes developed for problems with one space dimension in [34]. In particular, these methods were applied to antiplane problems in [16], which may be consulted for additional works on such problems by Garaizar and collaborators. We treat several important issues not treated by these authors: As part of the validation of our numerical solutions, we study axisymmetric problems. These of course have a polar singularity at the origin, which our methods readily handle. For dynamical problems, ingoing waves can focus at the origin [29] and could produce badly behaved solutions. (We show that this possibility does not occur for the problems we treat.) In solid mechanics, there are yet other phenomena in which the polar singularity interacts with material response. For example, [6] showed that certain nonlinearly elastic disks and balls could suffer (steady state) cavitation at the origin, in which a hole opens at the center when the outer boundary is subject to a sufficient amount of tension. The dynamical version of this phenomenon, involving focusing, exhibits a richer and not completely understood array of effects [27, 28]. These cavitational effects for symmetric problems depend on the response of the body to extension. But similar steady state effects hold for shear. Antman [2] showed that the qualitative behavior of a compressible elastic body under shear depended crucially on whether the (Piola–Kirchhoff) stress is super- or sublinear in the stretches for large stretches, with a serious singularity occuring for sublinear behavior. In order to investigate whether such phenomena could arise in our dynamical problems, we examine both super- and sublinear stress-strain laws. (The models of material response used by [32, 33] do not account for such growth.) We also carry out a careful validation of our methods, described below. For analyses of the Riemann problem see [15, 22, 30, 35].

Our method is robust and effective in capturing shocks and other kinds of sharp interfaces. It is our adaptation to the more complicated equations of nonlinear elasticity of methods widely used in gas dynamics [24, 26] which is a fundamental theme of our work. In particular, we compute shearing shocks in solids, which are not present in compressible fluids. (Strong shocks in gases are numerically treated in [38], for example).

Our work may be regarded as a first step toward devising effective methods for treating focusing effects for solids with nonlinear constitutive equations governed by equations with a hyperbolic character. Such solids include those described by theories of large-strain plasticity. Various steps in the numerical study of problems for such materials incorporate steps for elastic materials, which we are studying and validating here.

As part of our study, we examine the role of nonlinear constitutive assumptions. Our constitutive relations for shear give rise to isolated points at which the flux fails to be genuinely nonlinear in the sense of Lax [21]. At these points, detected during the computation, the numerical algorithm is modified. We treat several nonconvex flux functions (cf. [37]).

Among the methods recently developed for obtaining solutions in regions with boundaries of general shape are (i) Cartesian grid methods with a uniform rectangular computational mesh, for which the boundary of the domain is given special treatment inside the mesh [1, 9, 23]; (ii) the use of unstructured body-fitted grids of triangular or tetrahedral cells [36]; (iii) interpolation in a conservative manner on overlapping grids [10]; and (iv) the use of body-fitted structured grids [8, 17, 24]. We use the last method because it generally permits a more accurate treatment of the boundary conditions than (i) and it is easier to implement than (ii) or (iii). This method must be used with great care, however, to prevent solutions from being contaminated by the singularities of the coordinate transformations. We show how to do this.

We present examples showing that our numerical method is effective in capturing shocks that arise in systems of strictly hyperbolic conservation laws. (See [13] for other methods for systems of conservation laws.) Because of the nonlinearity of the equations, a closed-form, analytic solution is not available with which to compare the computed solution. Moreover, there are no available error estimates for our system. Consequently, we must carry out a rather intricate program, in which axisymmetric problems play a central role, to validate our results:

(i) We compute the analytic solution to an initial-boundary-value problem for the axisymmetric linear wave equation, on the unit disk, by separation of variables in polar coordinates. The axisymmetric initial data are supported on a smaller concentric disk.

(ii) We compute the solution of the same problem by our Godunov scheme. Agreement with the exact analytic solution of step (i) justifies the accuracy of the computed solution. These computations are delicate because of polar singularity at the origin.

(iii) We compute the solution to the initial-boundary-value problem in polar coordinates for the axisymmetric quasilinear wave equation, on the unit disk, with small initial data by the Godunov method, and compare this solution to that of the linear equation with the same data for small time. Since the solutions are in agreement for small time because of the initial linearity of the nonlinear problem, we compute with confidence the solution to axisymmetric quasilinear problems in one dimension by our Godunov scheme for a longer time.

(iv) We use the Godunov scheme with one-dimensional fluxes to compute the solution to the same initial-value-problem for the quasilinear wave equation in two-dimensional Cartesian coordinates on the unit square. Our methods do not exploit the axisymmetry. We validate this solution by comparing it to the solution of step (iii) up to the time that the waves hit the circular boundary of the unit disk. This problem enables us to make this comparison without worrying about boundary interactions.

(v) We compute the solution to the axisymmetric quasilinear problem for large times by our Godunov scheme with one-dimensional fluxes by using body-fitted coordinates, which do not exploit axisymmetry, on the unit disk with two independent spatial variables. We verify its accuracy by comparing its solutions with those of steps (iii) and (iv).

The development of this algorithm gives rise to numerical schemes capable of handling the polar singularity, which is a byproduct of our study of the axisymmetric problem (formulated in polar coordinates). The one-dimensional scheme that handles the axisymmetric problem is effective in calculating accurate solutions to the quasilinear wave equation and keeping the polar singularity under control. (The polar singularity, because of that of the coordinate system, does not arise in Cartesian coordinates.) **As our graphs show, the two-dimensional solutions accurately reproduce the profiles of the carefully constructed one-dimensional solutions**.

Section 2 gives a brief formulation of the antiplane shear problem of nonlinear elasticity and of the governing quasilinear hyperbolic system. In subsequent sections, we carry out steps (i)–(v).

2. THE ANTIPLANE SHEARING PROBLEM OF NONLINEAR ELASTICITY

Let $\{\mathbf{i}, \mathbf{j}, \mathbf{k}\}$ be an orthonormal basis for Euclidean 3-space. We identify a material point of a body by its position $x\mathbf{i} + y\mathbf{j} + z\mathbf{k}$ in a reference configuration of the body, or more simply, identify the material point by its Cartesian coordinates (x, y, z). Let $\mathbf{p}(x, y, z, t)$ denote the position of (x, y, z) at time t. We study deformations of an incompressible, homogeneous, isotropic, nonlinearly elastic body for which **p** has the form

$$\mathbf{p}(x, y, z, t) = x\mathbf{i} + y\mathbf{j} + [z + w(x, y, t)]\mathbf{k}. \tag{2.1}$$

In this very special kind of motion, each material point (x, y, z) can suffer only a “vertical” displacement $w(x, y, t)$ in the **k**-direction. Consequently, the motion is governed by a partial differential equation for the scalar w

$$w_{tt} = \left[\alpha\left(w_x^2 + w_y^2\right)w_x\right]_x + \left[\alpha\left(w_x^2 + w_y^2\right)w_y\right]_y \tag{2.2}$$

where subscripts denote partial derivatives, α is a given constitutive function of $w_x^2 + w_y^2$, and $\alpha(w_x^2 + w_y^2)w_x$ is the shear stress in the **k**-direction on a plane with normal **i** [3]. (It can be shown that for a given function α we can always obtain a stored-energy function satisfying Knowles’ [19] compatibility conditions for antiplane motions.) Equation (2.2) is virtually the only kind of exact *scalar* partial differential equation of motion for a deformable solid. As such, it furnishes a particularly convenient setting for numerical studies. Without loss of generality, we take the mass density to be 1.

The quasilinear wave equation (2.2), which gives a material (Lagrangian) description of the motion, is the object of our study.

3. PROBLEM FORMULATION IN POLAR COORDINATES

In this section, we seek axisymmetric solutions of (2.2) on the disk $\Omega = \{x, y : x^2 + y^2 \leq 1\}$ in the form

$$w(x, y) = \hat{w}(r) = \hat{w}(\sqrt{x^2 + y^2}), \quad r = \sqrt{x^2 + y^2}. \tag{3.1}$$

The substitution of (3.1) into (2.2) reduces it to

$$r w_{tt} = \left[r\alpha\left(w_r^2\right)w_r\right]_r, \tag{3.2}$$

where we have dropped the circumflex from w. We study (3.2) for $0 \leq r \leq 1$ subject to initial conditions of the form

$$w(r, 0) = W(r), \quad w_t(r, 0) = 0 \tag{3.3}$$

where W is prescribed, to the boundary condition

$$w(1, t) = 0, \tag{3.4}$$

and to the requirement that w be regular at $r = 0$.

We set

$$v = r w_t, \quad u = w_r \tag{3.5}$$

and define $f(u) = \alpha(u^2)u$. Thus, our initial-boundary-value problem is to solve

$$v_t = \{r f(u)\}_r, \quad u_t = (v/r)_r \tag{3.6}$$

subject to

$$u(0,t)=0, \qquad v(1,t)=0, \tag{3.7}$$

$$u(r,0)=W_r(r), \quad v(r,0)=0. \tag{3.8}$$

For compatibility, we require that $W(1)=0$.

The matrix version of (3.6) is

$$\mathbf{u}_t+\mathbf{f}(\mathbf{u},r)_r \equiv \mathbf{u}_t+\mathbf{A}\mathbf{u}_r+\mathbf{s}(\mathbf{u},r)=\mathbf{0} \tag{3.9}$$

where

$$\mathbf{u}=\begin{pmatrix} v \\ \mathrm{u} \end{pmatrix}, \qquad \mathbf{f}(\mathbf{u},r)=-\begin{pmatrix} rf(u) \\ v/r \end{pmatrix}, \tag{3.10}$$

$$\mathbf{A}=-\begin{pmatrix} 0 & rf_u \\ 1/r & 0 \end{pmatrix}, \quad \mathbf{s}(\mathbf{u},r)=\begin{pmatrix} -f(u) \\ v/r^2 \end{pmatrix}. \tag{3.11}$$

The eigenvalues λ_1, λ_2 of $\mathbf{A}$ are

$$\lambda_1=-\sqrt{f_u}, \quad \lambda_2=\sqrt{f_u}, \tag{3.12}$$

and the corresponding right and left eigenvectors of $\mathbf{A}$ are

$$\mathbf{r}_1=\begin{pmatrix} r\sqrt{f_u} \\ 1 \end{pmatrix}, \quad \mathbf{r}_2=\begin{pmatrix} -r\sqrt{f_u} \\ 1 \end{pmatrix}, \tag{3.13}$$

$$\mathbf{l}_1=(\mathrm{l},\ r\sqrt{f_u}), \quad \mathbf{l}_2=(1,\ -r\sqrt{f_u}). \tag{3.14}$$

Since

$$(\nabla_{\mathbf{u}}\lambda_1)\cdot\mathbf{r}_1=-\frac{f_{uu}}{2\sqrt{f_u}}, \quad (\nabla_{\mathbf{u}}\lambda_2)\cdot\mathbf{r}_2=\frac{f_{uu}}{2\sqrt{f_u}}, \tag{3.15}$$

system (3.6) is genuinely nonlinear in the sense of Lax where $f_{uu}\neq 0$. The flux function f, which is odd by definition, could be super- or sublinear for $u>0$. We consider only materials for which f_u is everywhere positive. Hence, our constitutive relations ensure that our problem is strictly hyperbolic [21].

3.1. *Numerical Formulation*

In this section, we describe the numerical algorithm used to obtain solutions of the system (3.6)–(3.8). We integrate the product of (3.6) with $1/r$ over a typical rectangle $[r^-, r^+]\times[t^-, t^+]$ to obtain

$$\int_{r^-}^{r^+}[u(r,t^+)-u(r,t^-)]\,dr=\int_{t^-}^{t^+}\left[\frac{v}{r}(r^+,t)-\frac{v}{r}(r^-,t)\right]dt, \tag{3.16}$$

$$\int_{r^-}^{r^+}[v(r,t^+)-v(r,t^-)]\,dr=\int_{t^-}^{t^+}[r^+f(u(r^+,t))-r^-f(u(r^-,t))]\,dt, \tag{3.17}$$

where $v = rw_t$. (These "impulse-momentum" laws are of course more fundamental than the classical equations (3.6).)

We formulate and implement a second-order Godunov-type scheme with a conservative finite-difference update that utilizes slope-limiting and explicit predictor-corrector time-stepping. Since this approach is also used in [5, 12], its description here will be brief.

We divide the domain [0, 1] into N cells $[r_{i-1}, r_i]$, $i = 1, \ldots, N$. Let $h_i = r_i - r_{i-1}$ be the length of each cell and $r_{i-1/2} = \frac{1}{2}(r_i + r_{i-1})$ be its midpoint. The numerical algorithm consists of the following procedures:

1. *Computation of the Time-Step.* The time-step is computed by taking into account the Courant–Friedrichs–Lewy (CFL) condition for shear waves. Specifically, the explicit stability bound is

$$\triangle t \leq K \frac{h_i}{c}, \tag{3.18}$$

where K is a constant less than 1, and c is the shear-wave speed. In our computations, we take $K = 0.7$.

The wave speeds $c = \pm\sqrt{f_u}$ are the eigenvalues of the matrix $\mathbf{A}$ and are approximated by the formula

$$\tilde{f}_u = \frac{f(u+\epsilon) - f(u-\epsilon)}{2\epsilon}, \tag{3.19}$$

which approaches "the wave speed" in the limit as $\epsilon \to 0$. The computed wave speeds at the cell centers are

$$\hat{c}_i^{n\pm} = c^{\pm}(u) = \pm\sqrt{\tilde{f}_u}. \tag{3.20}$$

Thus, the maximum stable time-step is computed by using

$$\triangle t \left[\max_i \frac{\tilde{c}_i^{n+}}{h_i} \right] \leq K. \tag{3.21}$$

2. *Slope Calculation and Limiting.* We maintain second-order accuracy of the computations by constructing slopes $\triangle\mathbf{u}_i^n$ from the solution $\mathbf{u}_k^n$ by using the piecewise linear profile

$$\mathbf{u}^n(r) = \mathbf{u}_i^n + \left(r - r_{i-1/2}\right)\triangle\mathbf{u}_i \quad \text{for } r_{i-1} < r < r_i. \tag{3.22}$$

Given the right eigenvectors $\{\mathbf{r}_k\}$ of $\mathbf{A}$, we express the central, forward, and backward differences of $\mathbf{u}$ as linear combinations of the $\mathbf{r}_k$

$$\begin{aligned} \frac{1}{2}(\mathbf{u}_{i+1} - \mathbf{u}_{i-1}) &= \sum m_k^c \mathbf{r}_k, \\ (\mathbf{u}_{i+1} - \mathbf{u}_i) &= \sum m_k^{\mathrm{r}} \mathbf{r}_k, \\ (\mathbf{u}_i - \mathbf{u}_{i-1}) &= \sum m_k^1 \mathbf{r}_k \end{aligned} \tag{3.23}$$

for $i = 1, \ldots, N$ and $k = 1, 2, 3$. Then $(\triangle\mathbf{u})_i = \sum m_k \mathbf{r}_k$ where

$$m_k = \begin{cases} \min\left\{\left|m_k^{\mathrm{c}}\right|, \gamma\left|m_k^1\right|, \gamma\left|m_k^{\mathrm{r}}\right|\right\}\operatorname{sgn}\left(m_k^{\mathrm{c}}\right) & \text{if } m_k^{\mathrm{r}} m_k^1 > 0, \\ 0, & \text{otherwise} \end{cases} \tag{3.24}$$

where γ is a parameter in the interval $[1, 2]$ that controls the implicitly added local viscosity. Throughout this paper, we take $\gamma = 2$, except in the presence of a local linear degeneracy, in which case, we set $\gamma = 1$ (cf. [7]).

3. *Prediction of the Solution.* In the predictor step, we advance the solution one half time-step by using a first-order approximation given by the explicit centered-difference formulas

$$u_i^{n+1/2} = u_i^n - \frac{\triangle t^n}{2h_i}[\tilde{v}(r_i^-)) - \tilde{v}(r_{i-1}^+))], \tag{3.25}$$

$$\tilde{v}_i^{n+1/2} = \tilde{v}_i^n - \frac{\triangle t^n}{2r_{i-1/2}h_i}[r_i f(u^n(r_i^-)) - r_{i-1} f(u^n(r_{i-1}^+))], \tag{3.26}$$

where $\tilde{v} = w_t$. We have slightly modified the standard formula derived from (3.17) in obtaining (3.26) in order to get an equation for $\tilde{v} = w_t$ rather than for $v = rw_t$. Second-order accuracy is recovered in the correction step, below.

4. *Computation of the Flux.* The computation of the flux is the most distinctive feature of the approximate Riemann solver of Davis. We define the values of $\mathbf{u}_\mathrm{L}$ and $\mathbf{u}_\mathrm{R}$ at the cell boundary r_i by

$$\mathbf{u}_\mathrm{L} = \mathbf{u}^{n+1/2}(r_i^-) = \mathbf{u}_i^{n+1/2} + \frac{1}{2}(\triangle\mathbf{u})_i, \tag{3.27}$$

$$\mathbf{u}_\mathrm{R} = \mathbf{u}^{n+1/2}(r_i^+) = \mathbf{u}_{i+1}^{n+1/2} - \frac{1}{2}(\triangle\mathbf{u})_{i+1}, \tag{3.28}$$

and the numerical average flux at r_i by

$$\hat{\mathbf{f}}_i^{n+1/2} = \hat{\mathbf{f}}_i^{n+1/2}\big(\mathbf{u}^{n+1/2}(r_i^-), \mathbf{u}^{n+1/2}(r_i^+)\big). \tag{3.29}$$

We compute upper and lower bounds on the wave speeds

$$c_{i,\mathrm{R}}^{n+1/2} = \max(c^+(\mathbf{u}_\mathrm{R}), c^+(\mathbf{u}_\mathrm{L})), \tag{3.30}$$

$$c_{i,\mathrm{L}}^{n+1/2} = -c_{i,\mathrm{R}}^{n+1/2}, \tag{3.31}$$

where c^+ is defined in Eq. (3.20). Hence, an approximation to the average flux across each cell boundary is

$$\hat{\mathbf{f}}_i^{n+1/2} = \frac{1}{2}\left[\mathbf{f}\big(\mathbf{u}^{n+1/2}(r_i^+)\big) + \mathbf{f}\big(\mathbf{u}^{n+1/2}(r_i^-)\big)\right] + \frac{1}{2}c_{i,R}^{n+1/2}\left[\mathbf{u}^{n+1/2}(r_i^-) - \mathbf{u}^{n+1/2}(r_i^+)\right]. \tag{3.32}$$

5. *Correction of the Solution.* Finally, the solution is corrected by using the flux approximations from Step (4) to obtain

$$\mathbf{u}_i^{n+1} = \mathbf{u}_i^n - \frac{\triangle t^n}{h_i}\big[\hat{\mathbf{f}}_i^{n+1/2} - \hat{\mathbf{f}}_{i-1}^{n+1/2}\big]. \tag{3.33}$$

As in the predictor step, we modify Eq. (3.17) for numerical coding. For more details of this algorithm, see [5, 12].

3.2. *Preliminary Numerical Results*

In this section, we present numerical results for different solutions to the nonlinear wave equation (3.2) given specific initial conditions and specific material behavior. We solve the system (3.6)–(3.8) with

$$N = 400, \quad K = 0.7, \tag{3.34}$$

with a quasilinear flux function of the form

$$f(w_r) = \alpha\left(w_r^2\right) w_r, \tag{3.35}$$

and with the following choices of $\alpha(w_r^2)$:

$$\alpha_1\left(w_r^2\right) = 1, \quad \alpha_2\left(w_r^2\right) = \frac{1}{\left(1 + w_r^2\right)^{1/4}}, \quad \alpha_3\left(w_r^2\right) = \sqrt{1 + w_r^2}. \tag{3.36}$$

The term f is respectively linear, sublinear, and superlinear for α_1, α_2, and α_3.

Before proceeding with steps (i)–(iii) in the Introduction (Section 1), we first validate the effectiveness of our scheme in capturing shocks. We briefly study the evolution of shear waves for a C^1 initial function W of the form

$$W(r) = \begin{cases} 2.5 \times 10^3 (r - 0.4)^2 (r - 0.6)^2, & 0.4 \le r \le 0.6, \\ 0, & \text{otherwise.} \end{cases} \tag{3.37}$$

so that

$$W_r(r) = \begin{cases} 10^4 (r - 0.4)(r - 0.5)(r - 0.6), & 0.4 \le r \le 0.6 \\ 0, & \text{otherwise.} \end{cases} \tag{3.38}$$

We compute the solution to the wave equation for these initial data (see Fig. 1a). For the linear wave equation ($\alpha = \alpha_1$) we do not obtain shocks, since the wave speeds are constant.

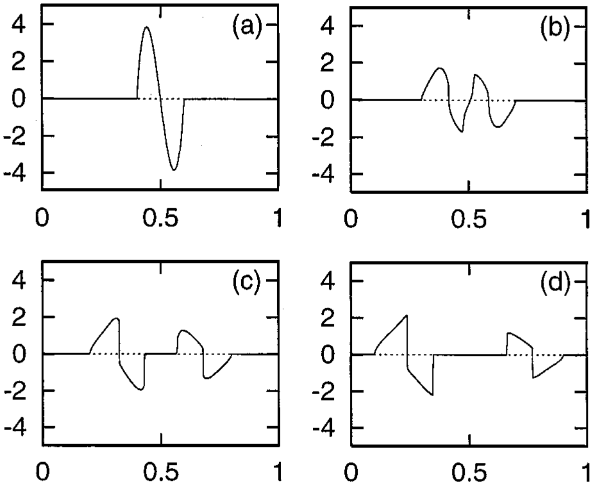

FIG. 1. The shear strain w_r computed with nonlinear flux function $\alpha = \alpha_2$. (a) $t = 0.0$, (b) $t = 0.1$, (c) $t = 0.2$, (d) $t = 0.3$.

For the nonlinear flux function with $\alpha = \alpha_2$, we obtain left- and right-moving shocks shown in Figs. 1c and 1d with the latter exhibiting fully developed N-waves. In refining the grid from $N = 400, 800$ to 1600, we find that the numerical method continues to capture the shock within four cells. Note that the speed of the wave at the back of the right-moving shock is greater than that of the wave speed in the front of the shock. The lack of symmetry of solutions about $r = \frac{1}{2}$ is of course due to the polar coordinates.

We now proceed with steps (i)–(iii) and consider the initial function

$$W(r) = \begin{cases} \frac{1}{4} - r^2 & \text{if } r \leq \frac{1}{2}, \\ 0 & \text{otherwise.} \end{cases} \tag{3.39}$$

We first consider the purely linear wave equation (with $\alpha = \alpha_1$) subject to the continuous initial data (3.39) which will demonstrate the effectiveness of our schemes in capturing shocks when $W_r(r)$ is discontinuous. The availability of an analytic solution for the initial-boundary-value problem (3.2)–(3.4) enables us to validate our solution constructed by the Godunov scheme. We initially compute our Godunov solution on annuli with tiny inner radii $\epsilon = 10^{-3}, 10^{-4}, 10^{-5}, 10^{-6}$, with the (natural) boundary condition $w_r(\epsilon, t) = 0$, to verify that possible singularities at the origin do not contaminate our numerical solutions. They do not. Indeed, the results for small ϵ are indistinguishable from those for $\epsilon = 0$, which we present here. (Care in handling the polar singularity in nonlinear elasticity is dictated by the appearance of surprising physical singularities at the origin for radially symmetric problems; cf. [3, 27, 28].)

The solution of this problem that is regular at the origin is

$$w(r, t) = \sum_{n=0}^{\infty} A_n J_0(\lambda_n r) \cos(\lambda_n t) \tag{3.40}$$

where

$$A_n = \frac{\int_0^1 r W(r) J_0(\lambda_n r)\, dr}{\int_0^1 r \{J_0(\lambda_n r)\}^2\, dr}. \tag{3.41}$$

Here $J_0(\xi)$ is Bessel's function of order zero, which satisfies the linear differential equation

$$\xi^2 R_{\xi\xi} + \xi R_\xi + \xi^2 R = 0, \tag{3.42}$$

and λ_n are the roots of $J_0(\lambda) = 0$, obtained from the boundary condition $w(1, t) = 0$.

In Fig. 2, we plot approximate solutions of our initial-value problem with initial data (3.39) obtained by (i) the Godunov scheme with (3.34) and (ii) a truncation to 100 terms of the series (3.40). Note that the agreement appears excellent except at the jumps. The series solution is superior in that it has sharper jumps, but it is inferior in that near the jumps, the graph is contaminated by the Gibbs phenomenon (cf. [18]).

There are small oscillations occurring at the origin (which are not discernible) in the plots of the displacement w versus r found by our Godunov scheme for nonlinear $\alpha = \alpha_2$ as the wave moves away from the origin and out toward the boundary. These oscillations are an effect of the singularity at $r = 0$ and are minimized by increasing the resolution near the origin. We have imposed the boundary condition $w_r(0, t) = 0$ to ensure regularity. Oscillations are not present in graphs of w_r (Fig. 3). The numerical scheme is capable of capturing the left- and right-moving waves. Note that the dissipative nature of the scheme

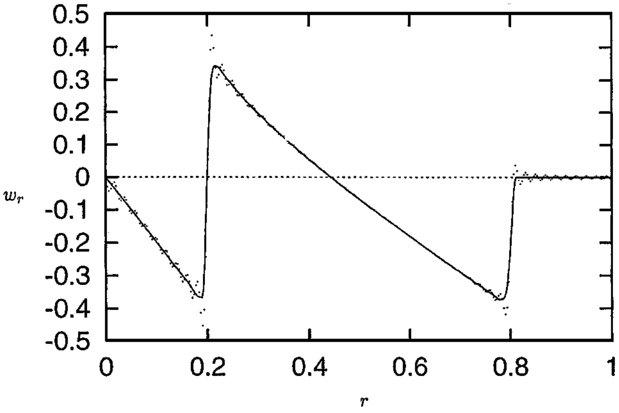

FIG. 2. The shear strain w_r as a function of r at $t = 0.3$ for the linear problem with initial condition (2.39). The solution computed by our Godunov scheme is plotted with the solid line and the truncation to 100 terms of the solution computed by separation of variables is plotted with the dotted line.

decreases the degree of steepness. When the left-moving discontinuity is reflected from the origin, it is inverted since the origin is an intact boundary. When the right-moving discontinuity is reflected from $r = 1$ it is not inverted, and it maintains its steepness until the two shocks interact, prior to $t = 1$.

To validate the accuracy of the numerical solution of the quasilinear problem, the results are compared to the solutions obtained numerically for the linear problem. For small data

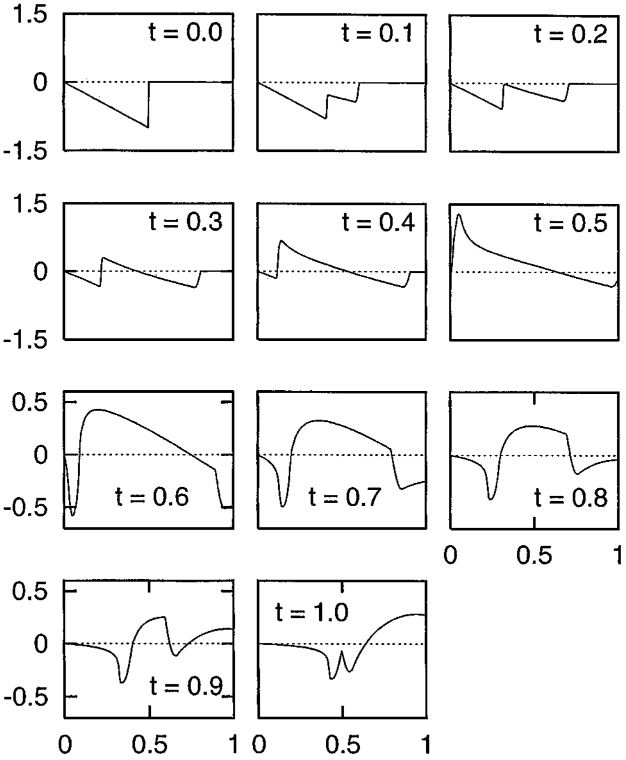

FIG. 3. The shear strain w_r versus r for nonlinear $\alpha = \alpha_2$ computed in polar coordinates at $t = 0.0$, $0.1, \ldots, 1.0$. Note that the scale changes at $t = 0.6$.

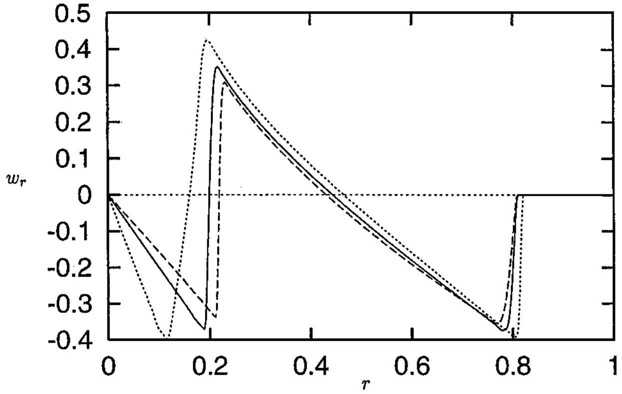

FIG. 4. The shear strain w_r versus r for (3.2) at $t = 0.3$ computed in polar coordinates with $\alpha = \alpha_1$ (solid line), α_2 (dashed line) and α_3 (dotted line).

and small evolution time, we expect the nonlinear solution to give results similar to those for the linear wave equation since the effects of the nonlinearity are not yet manifested. These solutions are in complete agreement for small data and small time (we omit the details).

Figure 4 is a spatial plot of w_r versus r at $t = 0.3$ for α_k, $k = 1, 2, 3$. In Fig. 4, we note that the wave speeds for superlinear α_3 are greater, thereby causing the wave to move faster toward the origin. Similarly, the plot for sublinear α_2 lags behind. The same phenomenon is present in plots of displacement, which have been omitted for space limitations. Note that the right-moving shock fronts for α_3 are much sharper than both the corresponding discontinuity for the linear equation ($\alpha = \alpha_1$), and the right-moving rarefaction wave for α_2. The converse is true for the left-moving shocks.

In analogy with our study of the Godunov scheme on annuli with small inner radius ϵ, it is instructive to study the solutions by separation of variables. Here we take the boundary condition on the inner radius to be $w_r(\epsilon, t) = 0$. By using standard properties of Bessel functions we find, just as for the Godunov schemes, that the solutions for small ϵ are indistinguishable from those for the complete disk. (The eigenvalues and eigenfunctions found in the solution process for small ϵ are themselves indistinguishable from those for the complete disk, in keeping with the Weyl theory of singular eigenvalue problems.)

4. PROBLEM FORMULATION IN CARTESIAN COORDINATES

In this section, we study (2.2) in Cartesian coordinates on the square $Q = \{x, y : -1 \leq x, y \leq 1\}$. We write (2.2) as

$$w_{tt} = f(w_x, w_y)_x + g(w_x, w_y)_y \tag{4.1}$$

with

$$f(w_x, w_y) = \alpha\left(w_x^2 + w_y^2\right)w_x, \quad g(w_x, w_y) = \alpha\left(w_x^2 + w_y^2\right)w_y. \tag{4.2}$$

By setting $u = w_x$, $z = w_y$, and $v = w_t$, we convert (4.1) to the first-order system

$$\begin{aligned} v_t &= f(u,z)_x + g(u,z)_y, \\ u_t &= v_x, \\ z_t &= v_y \end{aligned} \tag{4.3}$$

subject to initial conditions

$$w(x,y,0) = W(x,y), \quad v(x,y,0) = 0, \tag{4.4}$$

and boundary conditions

$$v(0,y,t) = 0 = v(1,y,t), \quad v(x,0,t) = 0 = v(x,1,t). \tag{4.5}$$

We write Eq. (4.3) as the matrix system

$$\mathbf{u}_t + \mathbf{f}_x + \mathbf{g}_y = \mathbf{0}, \tag{4.6}$$

where

$$\mathbf{u} = \begin{pmatrix} v \\ u \\ z \end{pmatrix}, \quad \mathbf{f} = -\begin{pmatrix} f(u,z) \\ v \\ 0 \end{pmatrix}, \quad \mathbf{g} = -\begin{pmatrix} g(u,z) \\ 0 \\ v \end{pmatrix}. \tag{4.7}$$

Consider the operator-split systems

$$\mathbf{u}_t + \mathbf{f}_x \equiv \mathbf{u}_t + \mathbf{A}\mathbf{u}_x = \mathbf{0}, \tag{4.8}$$

$$\mathbf{u}_t + \mathbf{g}_y \equiv \mathbf{u}_t + \mathbf{B}\mathbf{u}_y = \mathbf{0}, \tag{4.9}$$

where

$$\mathbf{A} = -\begin{pmatrix} 0 & f_u & f_z \\ 1 & 0 & 0 \\ 0 & 0 & 0 \end{pmatrix}, \quad \mathbf{B} = -\begin{pmatrix} 0 & g_u & g_z \\ 0 & 0 & 0 \\ 1 & 0 & 0 \end{pmatrix}. \tag{4.10}$$

We construct a solution of the full system from solutions of these by implementing an algorithm similar to that devised in Section 3.2 for the x and y problems. In particular, we approximate the fluxes for (4.8), (4.9) along the x- and y-coordinate lines successively (i.e., we compute the fluxes by looking at each direction separately). The method of alternately solving (4.8) and (4.9) is typically used in gas dynamics (where the equations are those of a degenerately elastic body) [38]. It is also implemented in the calculation of the time-steps and the slopes.

The eigenvalues of **A** are

$$\lambda_1^x = -\sqrt{f_u}, \quad \lambda_2^x = 0, \quad \lambda_3^x = \sqrt{f_u}, \tag{4.11}$$

and the corresponding right and left eigenvectors of $\mathbf{A}$ are

$$\mathbf{r}_1^x = \begin{pmatrix} \sqrt{f_u} \\ 1 \\ 0 \end{pmatrix}, \quad \mathbf{r}_2^x = \begin{pmatrix} 0 \\ -f_z \\ f_u \end{pmatrix}, \quad \mathbf{r}_3^x = \begin{pmatrix} -\sqrt{f_u} \\ 1 \\ 0 \end{pmatrix}, \tag{4.12}$$

$$\mathbf{l}_1^x = (\sqrt{f_u}, f_u, f_z), \quad \mathbf{l}_2^x = (0, 0, 1), \quad \mathbf{l}_3^x = (\sqrt{f_u}, -f_u, -f_z). \tag{4.13}$$

Thus,

$$\left(\nabla_{\mathbf{u}} \lambda_k^x\right) \cdot \mathbf{r}_k^x = \mp \frac{f_{uu}}{2\sqrt{f_u}}, \quad k = 1, 3, \tag{4.14}$$

so that (4.3) is genuinely nonlinear where $f_{uu} \neq 0$. Since $\lambda_2^x = 0$, the 2-wave is linearly degenerate.

Similarly, the eigenvalues of $\mathbf{B}$ are

$$\lambda_1^y = -\sqrt{g_z}, \quad \lambda_2^y = 0, \quad \lambda_3^y = \sqrt{g_z}, \tag{4.15}$$

and the corresponding right and left eigenvectors of $\mathbf{B}$ are

$$\mathbf{r}_1^y = \begin{pmatrix} \sqrt{g_z} \\ 0 \\ 1 \end{pmatrix}, \quad \mathbf{r}_2^y = \begin{pmatrix} 0 \\ -g_z \\ g_u \end{pmatrix}, \quad \mathbf{r}_3^y = \begin{pmatrix} -\sqrt{g_z} \\ 0 \\ 1 \end{pmatrix}, \tag{4.16}$$

$$\mathbf{l}_1^y = (\sqrt{g_z}, g_u, g_z), \quad \mathbf{l}_2^y = (0, 1, 0), \quad \mathbf{l}_3^y = (\sqrt{g_z}, -g_u, -g_z). \tag{4.17}$$

Thus,

$$\left(\nabla_{\mathbf{u}} \lambda_k^y\right) \cdot \mathbf{r}_k^y = \mp \frac{g_{zz}}{2\sqrt{g_z}}, \quad k = 1, 3, \tag{4.18}$$

so that (4.3) is genuinely nonlinear where $g_{zz} \neq 0$. Since $\lambda_2^y = 0$, the 2-wave is linearly degenerate. Also, we consider a reasonable class of materials for which $f_u \neq 0$ and $g_z \neq 0$. The functions $f(\cdot, z)$ and $g(u, \cdot)$ are odd and can have any growth; e.g., they could be superlinear or sublinear. If f_u or g_z should vanish at any point, the system (4.3) is nonstrictly hyperbolic and has an eigenvector deficiency. (The phenomenon of nonstrict hyperbolicity and eigenvector deficiencies, which greatly increases the difficulty of the numerics, is addressed in [7].)

4.1. *Numerical Formulation*

In this section, we formulate a Godunov-type method and numerically compute the solution to an initial-boundary-value problem for (2.2) on a square mesh. The data are such that the solution is axisymmetric for a while, but our formulation does not exploit this fact. This exercise corresponds to step (iv) of the Introduction (Section 1). This formulation is a two-dimensional extension of the method described in Section 3.1. The time-step restrictions are computed by using the appropriate time-steps for the operator-split systems. Similarly, the slopes are computed in the x- and y-directions separately.

We discretize the domain $[0, 1] \times [0, 1]$ into NM cells given by $[x_i, x_{i-1}] \times [y_j, y_{j-1}]$, $i = 1, \ldots, N$ and $j = 1, \ldots, M$. Let $h_i^x = x_i - x_{i-1}$ and $h_j^y = y_j - y_{j-1}$. The numerical algorithm is as follows:

1. *Computation of the Time-Step.* The time-step is computed for the x- and y-directions according to the explicit stability bound defined by the CFL condition (3.18). The minimum of $\triangle t_y$ and $\triangle t_x$ is taken as the global time-step $\triangle t^n$.

2. *Slope Calculation and Limiting.* For (4.8), slopes are computed along the x-coordinate lines from the solution $\mathbf{u}_{ij}^n$ by using a piecewise linear profile (3.22) in x. We now define $(\triangle_x \mathbf{u})_{ij} = \sum m_k \mathbf{r}_k^x$ where

$$m_k = \begin{cases} \min\{|m_k^{\mathrm{c}}|, \gamma|m_k^{\mathrm{l}}|, \gamma|m_k^{\mathrm{r}}|\}\operatorname{sgn}(m_k^{\mathrm{c}}) & \text{if } m_k^{\mathrm{r}} m_k^{\mathrm{l}} > 0, \\ 0, & \text{otherwise,} \end{cases} \tag{4.19}$$

and the m_k are defined by

$$\begin{aligned} \frac{1}{2}(\mathbf{u}_{i+1,j} - \mathbf{u}_{i-1,j}) &= \sum m_k^{\mathrm{c}} \mathbf{r}_k^x, \\ (\mathbf{u}_{i+1,j} - \mathbf{u}_{i,j}) &= \sum m_k^{\mathrm{r}} \mathbf{r}_k^x, \\ (\mathbf{u}_{i,j} - \mathbf{u}_{i-1,j}) &= \sum m_k^{\mathrm{l}} \mathbf{r}_k^x, \end{aligned} \tag{4.20}$$

which are the central, backward, and forward differences of $\mathbf{u}$. Equation (4.9) is treated similarly.

3. *Prediction of the Solution.* In the predictor step, we advance the solution one half time-step by using a first-order approximation given by the explicit centered-difference formula

$$\begin{aligned} \mathbf{u}_{ij}^{n+1/2} = \mathbf{u}_{ij}^n &- \frac{\triangle t^n}{2h_i^x}\left[\mathbf{f}\left(\mathbf{u}\left(x_i^-, y_{j-1/2}\right)\right) - \mathbf{f}\left(\mathbf{u}\left(x_{i-1}^+, y_{j-1/2}\right)\right]\right. \\ &- \frac{\triangle t^n}{2h_i^y}\left[\mathbf{g}\left(\mathbf{u}\left(x_{i-1/2}, y_j^-\right)\right) - \mathbf{g}\left(\mathbf{u}\left(x_{i-1/2}, y_{j-1}^+\right)\right)\right]. \end{aligned} \tag{4.21}$$

Here, predicted fluxes $\mathbf{f}(\mathbf{u}(\cdot, y_{j-1/2}))$ are computed along y-coordinate lines while the $\mathbf{g}(\mathbf{u}(x_{i-1/2}, \cdot))$ are computed along x-coordinate lines. (Second-order accuracy is recovered in the correction step, described below.)

4. *Computation of the Flux.* In two dimensions, it is necessary to compute an approximate average flux at (x_i, y_j). In order to do this, we define the value of $\mathbf{u}$ at the cell boundaries by

$$\mathbf{u}_{\mathrm{L}} = \mathbf{u}^{n+1/2}\left(x_i^-, y_{j-1/2}\right) = \mathbf{u}_{i,j}^{n+1/2} + \frac{1}{2}(\triangle_x \mathbf{u})_{i,j}, \tag{4.22}$$

$$\mathbf{u}_{\mathrm{R}} = \mathbf{u}^{n+1/2}\left(x_i^+, y_{j-1/2}\right) = \mathbf{u}_{i+1,j}^{n+1/2} - \frac{1}{2}(\triangle_x \mathbf{u})_{i+1,j}, \tag{4.23}$$

$$\mathbf{u}_{\mathrm{B}} = \mathbf{u}^{n+1/2}\left(x_{i-1/2}, y_j^-\right) = \mathbf{u}_{i,j}^{n+1/2} + \frac{1}{2}(\triangle_y \mathbf{u})_{i,j}, \tag{4.24}$$

$$\mathbf{u}_{\mathrm{T}} = \mathbf{u}^{n+1/2}\left(x_{i-1/2}, y_j^+\right) = \mathbf{u}_{i,j+1}^{n+1/2} - \frac{1}{2}(\triangle_y \mathbf{u})_{i,j+1}, \tag{4.25}$$

and the numerical average fluxes at (x_i, y_j) by

$$\hat{\mathbf{f}}_{ij}^{n+1/2} = \hat{\mathbf{f}}_{ij}^{n+1/2}\left(\mathbf{u}^{n+1/2}\left(x_i^-, y_{j-1/2}\right), \mathbf{u}^{n+1/2}\left(x_i^+, y_{j-1/2}\right)\right), \tag{4.26}$$

$$\hat{\mathbf{g}}_{ij}^{n+1/2} = \hat{\mathbf{g}}_{ij}^{n+1/2}\left(\mathbf{u}^{n+1/2}\left(x_{i-1/2}, y_j^-\right), \mathbf{u}^{n+1/2}\left(x_{i-1/2}, y_j^+\right)\right). \tag{4.27}$$

We compute upper and lower bounds on the wave speeds

$$c_{i,\mathrm{R}}^{n+1/2} = \max(c^+(\mathbf{u}_\mathrm{R}), c^+(\mathbf{u}_\mathrm{L})), \tag{4.28}$$

$$c_{j,\mathrm{T}}^{n+1/2} = \max(c^+(\mathbf{u}_\mathrm{T}), c^+(\mathbf{u}_\mathrm{B})), \tag{4.29}$$

where in Eq. (4.28) c^+ is computed by using Eq. (3.20), and in Eq. (4.29) c^+ is computed by using the analogous

$$\hat{c}_j^{n\pm} = c^\pm(u, z) = \pm\sqrt{\tilde{g}_z}. \tag{4.30}$$

Hence, approximations to the average fluxes across each cell boundary are

$$\begin{aligned}\hat{\mathbf{f}}_{ij}^{n+1/2} &= \frac{1}{2}\left[\mathbf{f}\left(\mathbf{u}^{n+1/2}\left(x_i^+, y_{j-1/2}\right)\right) + \mathbf{f}\left(\mathbf{u}^{n+1/2}\left(x_i^-, y_{j-1/2}\right)\right)\right]\\ &\quad + \frac{1}{2}c_{i,\mathrm{R}}^{n+1/2}\left[\mathbf{u}^{n+1/2}\left(x_i^-, y_{j-1/2}\right) - \mathbf{u}^{n+1/2}\left(x_i^+, y_{j-1/2}\right)\right],\end{aligned} \tag{4.31}$$

$$\begin{aligned}\hat{\mathbf{g}}_{ij}^{n+1/2} &= \frac{1}{2}\left[\mathbf{g}\left(\mathbf{u}^{n+1/2}\left(x_{i-1/2}, y_j^+\right)\right) + \mathbf{f}\left(\mathbf{u}^{n+1/2}(x_{i-1/2}, y_j^-)\right)\right]\\ &\quad + \frac{1}{2}c_{j,\mathrm{T}}^{n+1/2}\left[\mathbf{u}^{n+1/2}\left(x_{i-1/2}, y_j^-\right) - \mathbf{u}^{n+1/2}\left(x_{i-1/2}, y_j^+\right)\right],\end{aligned} \tag{4.32}$$

5. *Correction of the Solution.* The solution is corrected by using the flux approximations to obtain

$$\mathbf{u}_{ij}^{n+1} = \mathbf{u}_{ij}^n - \frac{\triangle t^n}{h_i^x}\left[\hat{\mathbf{f}}_{ij}^{n+1/2} - \hat{\mathbf{f}}_{i-1,j}^{n+1/2}\right] - \frac{\triangle t^n}{h_j^y}\left[\hat{\mathbf{g}}_{ij}^{n+1/2} - \hat{\mathbf{g}}_{i,j-1}^{n+1/2}\right]. \tag{4.33}$$

Note that the scheme is posed in unsplit form even though the flux approximations are computed by using the operator-split formulation.

We discuss solutions based this formulation in Section 6.

5. PROBLEM FORMULATION IN BODY-FITTED CURVILINEAR COORDINATES

In this section, we begin our treatment of step (v) of the Introduction (Section 1) by formulating (2.2) on the unit disk $\Omega = \{x, y : x^2 + y^2 < 1\}$. We begin with a description of the mesh transformation for any domain Ω which is diffeomorphic to a unit square.

5.1. *The Transformation*

Consider the transformation $x = x(\xi, \eta)$, $y = y(\xi, \eta)$ from the computational rectangle $R = \{\xi, \eta : 0 < \xi < M,\ 0 < \eta < N\}$, where M and N are positive integers, to the physical domain Ω. The transformation gradient may be expressed as

$$\begin{aligned}\begin{pmatrix}\partial/\partial x\\ \partial/\partial y\end{pmatrix} &= \frac{1}{x_\xi y_\eta - x_\eta y_\xi}\begin{pmatrix} y_\eta & -y_\xi\\ -x_\eta & x_\xi\end{pmatrix}\begin{pmatrix}\partial/\partial\xi\\ \partial/\partial\eta\end{pmatrix}\\ &\equiv \frac{1}{J}\begin{pmatrix} q_1 & s_1\\ q_2 & s_2\end{pmatrix}\begin{pmatrix}\partial/\partial\xi\\ \partial/\partial\eta\end{pmatrix} \equiv \frac{1}{J}(\mathbf{qs})\begin{pmatrix}\partial/\partial\xi\\ \partial/\partial\eta\end{pmatrix},\end{aligned} \tag{5.1}$$

where $J = x_\xi y_\eta - x_\eta y_\xi$ is the Jacobian of the transformation.

5.2. *Transformed System*

As in Section 4, let $u = w_x$, $z = w_y$, $v = w_t$. Then (2.2) may be expressed as (cf. 4.3)

$$\begin{aligned} v_t - (\alpha(u, z)u)_x - (\alpha(u, z)z)_y &= 0, \\ u_t - v_x &= 0, \\ z_t - v_y &= 0. \end{aligned} \tag{5.2}$$

Applying the transformation (5.1) to (5.2) we obtain

$$\begin{aligned} J\tilde{v}_t - q_1(\alpha(\tilde{u}, \tilde{z})\tilde{u})_\xi - q_2(\alpha(\tilde{u}, \tilde{z})\tilde{z})_\xi - s_1(\alpha(\tilde{u}, \tilde{z})\tilde{u})_\eta - s_2(\alpha(\tilde{u}, \tilde{z})\tilde{z})_\eta &= 0, \\ J\tilde{u}_t - q_1\tilde{v}_\xi - s_1\tilde{v}_\eta &= 0, \\ J\tilde{z}_t - q_2\tilde{v}_\xi - s_2\tilde{v}_\eta &= 0, \end{aligned} \tag{5.3}$$

where $\tilde{f}(\xi, \eta) = f(x(\xi, \eta), y(\xi, \eta))$. Equation (5.3) can be expressed in conservative form as

$$\begin{aligned} J\tilde{v}_t - (\alpha(\tilde{u}, \tilde{z})(q_1\tilde{u} + q_2\tilde{z}))_\xi - (\alpha(\tilde{u}, \tilde{z})(s_1\tilde{u} + s_2\tilde{z}))_\eta &= 0, \\ J\tilde{u}_t - (q_1\tilde{v})_\xi - (s_1\tilde{v})_\eta &= 0, \\ J\tilde{z}_t - (q_2\tilde{v})_\xi - (s_2\tilde{v})_\eta &= 0, \end{aligned} \tag{5.4}$$

where we have explicitly used the fact that

$$\mathbf{q}_\xi + \mathbf{s}_\eta = \mathbf{0}, \tag{5.5}$$

which follows immediately from (5.1). The equations (5.4) are now in the same format as the system (4.6) (with ξ, η replacing x, y and with the factor J multiplying the time derivatives.) Note that the flux functions

$$\mathbf{f} = \begin{pmatrix} f_1 \\ f_2 \\ f_3 \end{pmatrix}, \quad \mathbf{g} = \begin{pmatrix} g_1 \\ g_2 \\ g_3 \end{pmatrix} \tag{5.6}$$

have new definitions.

5.3. *Discretized Metric Coefficients*

In the computational space, the grid cells are unit squares with vertices $(\xi_i, \eta_j) = (i, j)$ for $i = 0, \ldots, M$ and $j = 0, \ldots, N$. Discrete values of $\mathbf{q}$ are defined at the centers of the vertical edges of the unit squares, while discrete values for $\mathbf{s}$ are defined at the centers of the horizontal edges by

$$\mathbf{q}_{i,j+1/2} = \begin{pmatrix} y_{i,j+1} - y_{i,j} \\ -(x_{i,j+1} - x_{i,j}) \end{pmatrix} \quad \text{for } i = 0, \ldots, M,\ j = 0, \ldots, N-1, \tag{5.7}$$

$$\mathbf{s}_{i+1/2,j} = \begin{pmatrix} -(y_{i+1,j} - y_{i,j}) \\ x_{i+1,j} - x_{i,j} \end{pmatrix} \quad \text{for } i = 0, \ldots, M-1,\ j = 0, \ldots, N, \tag{5.8}$$

$$x_{ij} = x(\xi_i, \eta_j), \quad y_{ij} = y(\xi_i, \eta_j). \tag{5.9}$$

Note that

$$\mathbf{q}_{i+1,j+1/2} - \mathbf{q}_{i,j+1/2} + \mathbf{s}_{i+1/2,j+1} - \mathbf{s}_{i+1/2,j} = \mathbf{0}, \tag{5.10}$$

is true for $i = 0, \ldots, M-1$ and $j = 0, \ldots, N-1$, corresponding to a centered difference approximation to (5.5) at the center of each cell. This property is important in preserving second-order spatial accuracy of the transformed conservation equations. The Jacobian is defined at cell centers by using centered difference approximations for each derivative term based on the values at the four corners of each cell.

5.4. *Grid Generation*

To generate a grid on a (simply-connected) planar region Ω we first divide its boundary $\partial\Omega$ into four separate curves, which are described parametrically by functions $[0,1] \ni \xi \mapsto \mathbf{x}_\mathrm{b}(\xi), \mathbf{x}_\mathrm{t}(\xi)$, $[0,1] \ni \eta \mapsto \mathbf{x}_\mathrm{l}(\eta), \mathbf{x}_\mathrm{r}(\eta)$ [20]. (The subscripts b, t, l, r stand for bottom, top, left, right of the square $\{\xi, \eta : 0 < \xi < 1, 0 < \eta < 1\}$ into which Ω is going to be mapped.) For our problem, we take

$$\begin{aligned} \mathbf{x}_\mathrm{t}(\xi) &= \begin{pmatrix} x_\mathrm{t}(\xi) \\ y_\mathrm{t}(\xi) \end{pmatrix} = \begin{pmatrix} (2\xi - 1)/\sqrt{2} \\ \sqrt{1 - x_\mathrm{t}(\xi)^2} \end{pmatrix}, \\ \mathbf{x}_\mathrm{r}(\eta) &= \begin{pmatrix} x_\mathrm{r}(\eta) \\ y_\mathrm{r}(\eta) \end{pmatrix} = \begin{pmatrix} \sqrt{1 - y_\mathrm{r}(\eta)^2} \\ (2\eta - 1)/\sqrt{2} \end{pmatrix}, \ldots. \end{aligned} \tag{5.11}$$

We map the square $\{\xi, \eta : 0 < \xi < 1, 0 < \eta < 1\}$ to Ω by the function $\hat{\mathbf{x}}$ defined by the interpolation formula [20]

$$\begin{aligned} \hat{\mathbf{x}}(\xi, \eta) = {} & (1-\eta)\mathbf{x}_\mathrm{b}(\xi) + \eta\mathbf{x}_\mathrm{t}(\xi) + (1-\xi)\mathbf{x}_\mathrm{l}(\eta) + \xi\mathbf{x}_\mathrm{r}(\eta) - \{\xi\eta\mathbf{x}_\mathrm{t}(1) \\ & + \xi(1-\eta)\mathbf{x}_\mathrm{b}(1) + \eta(1-\xi)\mathbf{x}_\mathrm{t}(0) + (1-\xi)(1-\eta)\mathbf{x}_\mathrm{b}(0)\}. \end{aligned} \tag{5.12}$$

We now define our mapping $\mathbf{x}$ of R to Ω by $\mathbf{x}(\xi, \eta) \equiv \hat{\mathbf{x}}(\xi/M, \eta/N)$. The grid on Ω, illustrated in Fig. 5, has intersection points at $\mathbf{x}(i, j)$, and the curves constituting the grid in Ω are given by $\xi \mapsto \mathbf{x}(\xi, j)$ and $\eta \mapsto \mathbf{x}(i, \eta)$.

5.5. *Boundary Conditions*

Boundary conditions are implemented by specifying appropriate values for the fluxes on cell faces that form part of the boundary. For example, the condition $\tilde{v} = 0$ at the boundary implies that

$$(f_2)_{0,j+1/2} = (f_3)_{0,j+1/2} = (f_2)_{M,j+1/2} = (f_3)_{M,j+1/2} = 0, \tag{5.13}$$

$$(g_2)_{i+1/2,0} = (g_3)_{i+1/2,0} = (g_2)_{i+1/2,N} = (g_3)_{i+1/2,N} = 0 \tag{5.14}$$

for $i = 0, \ldots, M-1$ and $j = 0, \ldots, N-1$. Boundary values for the fluxes f_1 and g_1 corresponding to the first equation in (5.4) are less obvious. Since $\tilde{v} = 0$ on ∂R, it follows from (5.4) that some approximation to $(f_1)_\xi + (g_1)_\eta = 0$ should also be imposed. For example, along the boundary $i = M$, the function f_1 is determined by using

$$(f_1)_{M,j+1/2} = (f_1)_{M-1,j+1/2} - (g_1)_{M+1/2,j+1} + (g_1)_{M+1/2,j} \tag{5.15}$$

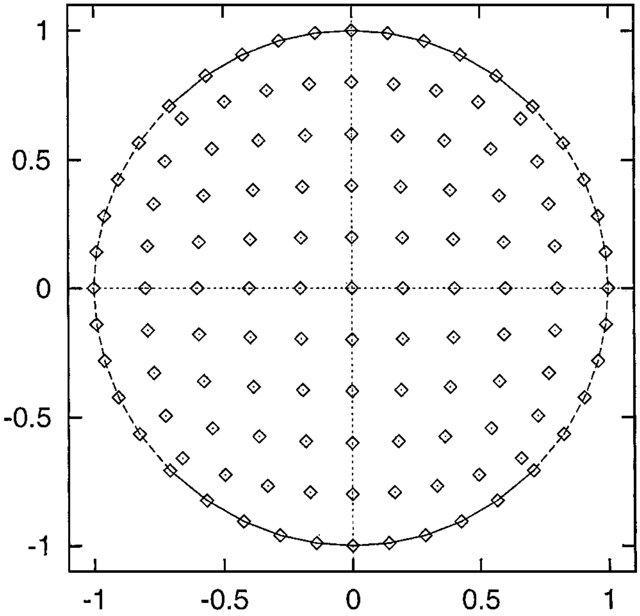

FIG. 5. The physical grid discretized by using (5.11) and (5.12) for $N = M = 10$. The top and bottom boundaries $\mathbf{x}_t$ and $\mathbf{x}_b$ are plotted with solid lines. The left and right boundaries $\mathbf{x}_l$ and $\mathbf{x}_r$ are plotted with dashed lines.

for $j = 0, \ldots, N-1$, with similar formulas along the boundaries $i = 0$, $j = 0$ and $j = N$. We remark that this specification of the fluxes is equivalent to setting $\tilde{v} = 0$ inside all the cells adjacent to the boundary and hence is only a first-order accurate treatment **only at the boundary and only where there are severe distortions of the grid**. This treatment of boundary conditions removes spurious oscillations appearing as a wave approaches the boundary along a diagonal when the problem is treated by the technique mentioned in the next subsection. This instability is caused by the severity of the grid distortion near these points.

5.6. *Faulty Alternative Formulations*

We conclude Section 5 with a warning about the formulation of Eq. (2.2) in generalized coordinates. Following [20, 25, 31] we may first transform (2.2) into generalized coordinates and then express it as the system

$$\begin{aligned} Jv_t &= f(u(\xi,\eta,t), z(\xi,\eta,t), \xi, \eta)_\xi + g(u(\xi,\eta,t), z(\xi,\eta,t), \xi, \eta)_\eta, \\ u_t &= v_\xi, \\ z_t &= v_\eta \end{aligned} \tag{5.16}$$

where

$$\begin{gathered} f = \hat{\alpha}\hat{w}_\xi + \hat{\beta}\hat{w}_\eta, \quad g = \hat{\beta}\hat{w}_\xi + \hat{\gamma}\hat{w}_\eta, \\ \hat{\alpha} = \frac{\tilde{\alpha}}{J}\left(y_\eta^2 + x_\eta^2\right), \quad \hat{\beta} = -\frac{\tilde{\alpha}}{J}(y_\xi y_\eta + x_\xi x_\eta), \quad \hat{\gamma} = \frac{\tilde{\alpha}}{J}\left(y_\xi^2 + x_\xi^2\right), \\ v = \tilde{w}_t, \quad u = \tilde{w}_\xi, \quad z = \tilde{w}_\eta. \end{gathered} \tag{5.17}$$

Note that the evaluation of the discrete fluxes in this formulation requires that all metric coefficients be defined at all four cell edges. Thus, the simple discretizations (5.7) and (5.8) do not suffice in this formulation. We have experimented with several discretizations of the metric coefficients using this formulation including central differences and the use of "exact" derivatives obtained from differentiating (5.12) explicitly. In all tests, spurious oscillations appear near the intersection of the boundary and the diagonals $y = \pm x$, where the grid is severely distorted. These oscillations, which destroy the axisymmetry, are illustrated in Fig. 12.

6. NUMERICAL RESULTS

In this section, we present computations supporting the effectiveness of the numerical method in two dimensions. We consider the following cases which correspond to (3.36):

$$\begin{gathered}\alpha_1\left(w_x^2 + w_y^2\right) = 1, \quad \alpha_2\left(w_x^2 + w_y^2\right) = \frac{1}{\left(1 + w_x^2 + w_y^2\right)^{1/4}}, \\ \alpha_3\left(w_x^2 + w_y^2\right) = \sqrt{1 + w_x^2 + w_y^2}.\end{gathered} \tag{6.1}$$

We shall solve systems (4.3) and (5.4) with the following choice of parameters:

$$N = M = 200, \quad K = 0.5, \tag{6.2}$$

$$W(x, y) = \begin{cases} \frac{1}{4} - x^2 - y^2 & \text{if } x^2 + y^2 \leq \frac{1}{4}, \\ 0 & \text{otherwise.} \end{cases} \tag{6.3}$$

As in the model formulated in polar coordinates, we first compute the analytic solution to the linear wave equation (4.1) (for which $\alpha = \alpha_1 = 1$) by separation of variables subject to initial and boundary conditions

$$w(0, y, t) = 0 = w(1, y, t), \quad w_y(x, 0, t) = 0 = w_y(x, 1, t) \tag{6.4}$$

$$w(x, y, 0) = W(x, y), \quad w_t(x, y, 0) = 0. \tag{6.5}$$

Hence,

$$w(x, y, t) = \sum_{n=1}^{\infty} \sum_{m=0}^{\infty} A_{nm} \Psi_{nm} \cos \sqrt{n^2 + m^2 t}, \tag{6.6}$$

where $\Psi_{nm} = \sin(n\pi x)\cos(m\pi y)$ and

$$A_{nm} = \frac{\int_0^1 \int_0^1 W(x, y)\Psi_{nm}\, dx\, dy}{\int_0^1 \int_0^1 \Psi_{nm}^2\, dx\, dy}. \tag{6.7}$$

The solution is then calculated in Cartesian coordinates by using the second-order Godunov scheme to obtain partial verification of the accuracy of the scheme. We find results similar to those in the one-dimensional evaluation: The solutions are in agreement and the series solution exhibits oscillations near the discontinuities. These figures have been omitted.

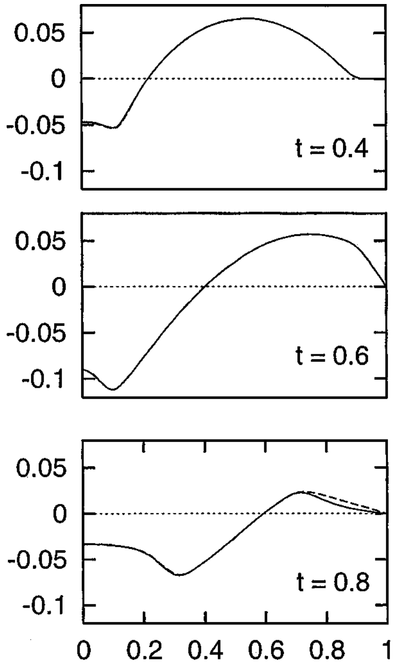

FIG. 6. The displacement w versus r for the quasilinear wave equation with $\alpha = \alpha_2$ at $t = 0.4$, 0.6, and 0.8. The solution computed using polar coordinates is plotted with the solid line and the Cartesian coordinate solution is plotted with the dashed line. Boundary interactions first occur near $t = 0.48$. Note that the solutions coincide until effects of the boundary interactions are significant.

We now focus on the verification of two-dimensional results by comparing solutions computed in Cartesian coordinates and the body-fitted curvilinear coordinates with those obtained in polar coordinates. Our first results are restricted to the two-dimensional solution on the square Q. We compute the solution to the linear wave equation ($\alpha = \alpha_1$) and the quasilinear wave equation ($\alpha = \alpha_2$) in Cartesian coordinates on Q with initial function (6.3), corresponding to (3.39), which is supported on a small disk.

Figure 6 is a plot of the displacement w versus r for the axisymmetric problem computed in polar coordinates and the same problem computed in Cartesian coordinates at various times. Note that the solutions are in agreement until the right-moving wave first hits the right boundary. Since the problem solved on the square does not impose axisymmetric boundary conditions, we see that the solutions diverge once interaction with the boundary takes place. This agreement, up until interaction, supports the accuracy of the two-dimensional scheme on the square. We conclude that the two-dimensional solution obtained using Cartesian coordinates is extremely accurate prior to boundary interactions.

To conclude this analysis, we study the fully two-dimensional computation of the solution by a Godunov-type scheme on the disk on a time interval large enough for boundary interactions to come into play. For this solution, we used the formulation (5.1)–(6.5). Our boundary conditions corresponding to (3.7) are

$$v(0, \eta, t) = 0 = v(1, \eta, t), \quad v(\xi, 0, t) = 0 = v(\xi, 1, t). \tag{6.8}$$

Figures 7 and 8 exhibit the vertical displacement w versus r, computed by our three different approaches with $\alpha = \alpha_2$ at $t = 0.3$. In the illustrations, P, C, and B denote solutions

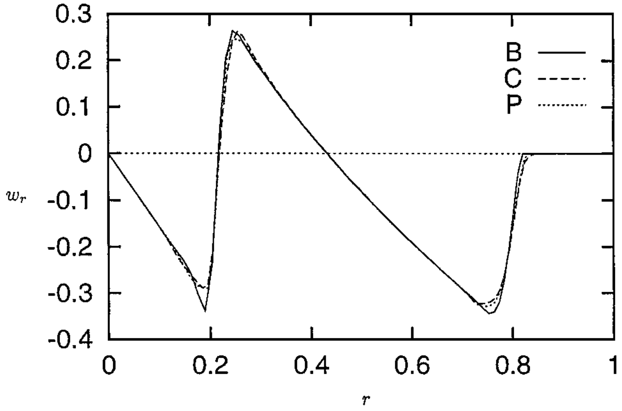

FIG. 7. The shear strain w_r versus r for the axisymmetric quasilinear problem ($\alpha = \alpha_2$) at $t = 0.3$ computed in one dimension using polar coordinates (P), and in two dimensions using Cartesian coordinates (C) and body-fitted coordinates (B).

computed using polar coordinates, Cartesian coordinates, and body-fitted curvilinear coordinates, respectively. Solutions computed using the body-fitted coordinates are displayed along the line $y = x$. Virtually identical results are found along the x and y axes prior to boundary interactions. Solutions displayed in polar coordinates are computed with 100 points. In Fig. 7 the numerical method captures the left-moving shock within approximately four cells.

It is clear that the two-dimensional numerical scheme in Cartesian and body-fitted coordinates is capable of computing accurate solutions. Of course, we expect the solutions to diverge once interaction with the boundary occurs. We also expect some disagreement in the solution computed by using body-fitted coordinates since the boundary is artificially approximated by a finite number of mesh points.

Figure 9, however, shows how the solution computed with the body-fitted coordinates agrees closely with the polar coordinate solution after interaction with the boundary. We also conclude that the two-dimensional second-order Godunov scheme is capable of calculating

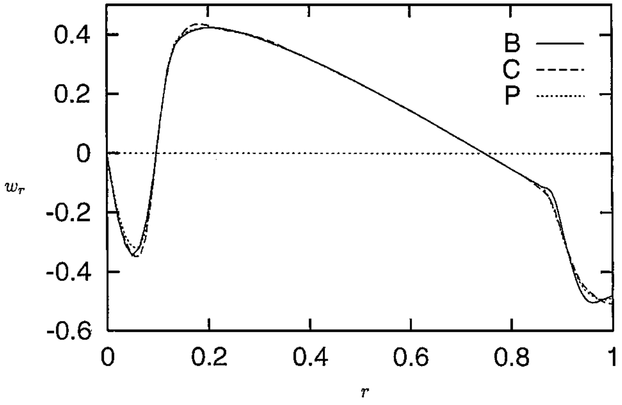

FIG. 8. The shear strain w_r versus r for the axisymmetric quasilinear problem ($\alpha = \alpha_2$) at $t = 0.6$ computed in one dimension using polar coordinates (P), and in two dimensions using Cartesian coordinates (C), and body-fitted coordinates (B).

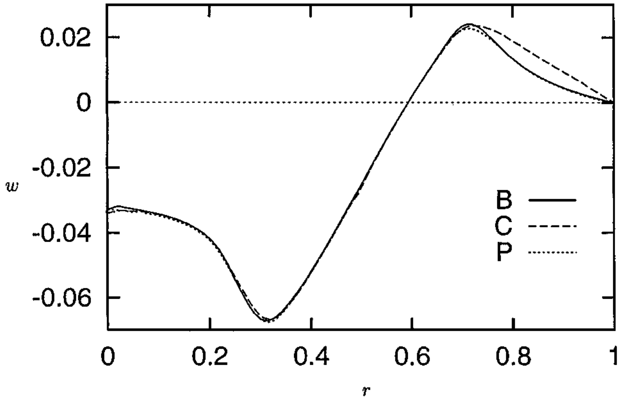

FIG. 9. The displacement w versus r for the axisymmetric quasilinear problem ($\alpha = \alpha_2$) at $t = 0.8$ computed in one dimension using polar coordinates (P), and in two dimensions using Cartesian coordinates (C), and body-fitted coordinates (B). Note that the Cartesian formulation is not accurate because of boundary interactions.

accurate solutions when nonconvex constitutive relations are incorporated. Figures 10 and 11 show the three-dimensional graphs of w_r at two different times for $\alpha = \alpha_3$. These figures indicate how-effectively axisymmetry is preserved even though the numerical scheme did not account for it.

Finally, let us describe what happened we computed the solution to (2.2) in the two-dimensional generalized body-fitted coordinates using the faculty alternative formulation based on (5.16). The boundary conditions (5.13)–(5.15) were expressed in terms of the variables of this system. In each case, the solutions computed for $\alpha = \alpha_1, \alpha_2, \alpha_3$ for $0 \leq t \leq 1$ and for various N and M, *when restricted to the x-axis* are in excellent agreement with the polar coordinate solution before and after boundary interactions. Moreover, the solution on the x-axis continues to converge to the polar coordinates solution for fixed x, t as grid refinements are performed.

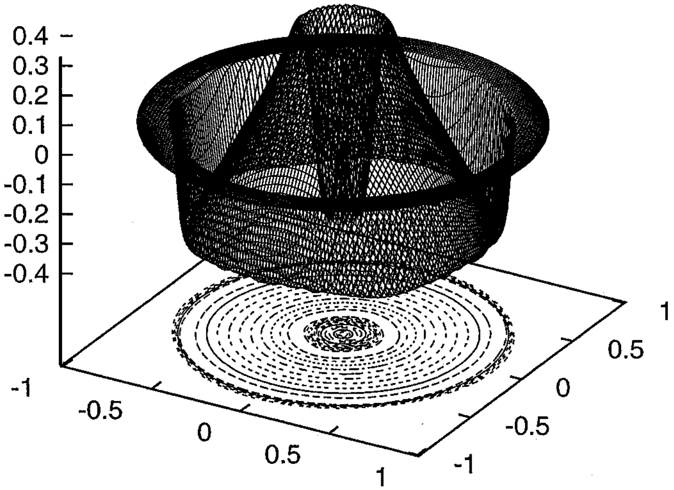

FIG. 10. Graph of the shear strain w_r plotted over the (x, y)-plane plane with 200 mesh points for the axisymmetric quasilinear problem ($\alpha = \alpha_3$) in body-fitted coordinates at the time $t = 0.3$. The contour lines are shown in the (x, y)-plane.

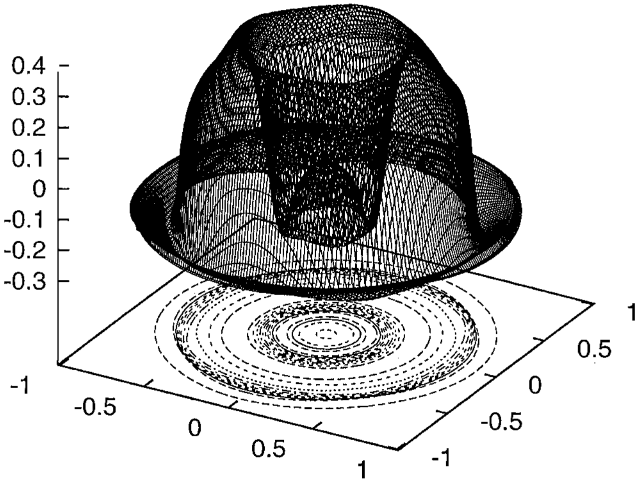

FIG. 11. Graph of the shear strain w_r plotted over the (x, y)-plane plane with 200 mesh points for the axisymmetric quasilinear problem ($\alpha = \alpha_3$) in body-fitted coordinates at the time $t = 0.7$. The contour lines are shown in the (x, y)-plane.

On the other hand, the restriction of the solution to the lines $y = \pm x$ closely match the polar-coordinate solution only up to the time of boundary interactions. Thereafter, this agreement ceases and the boundary conditions fail to be satisfied at the corresponding boundary points because of severe oscillations. Moreover, we found that the instability near these boundary points increases severely (because of the distortion of the grid) as the computational grid is refined. Thus, axisymmetry, a main criterion for evaluating the effectiveness of our numerical schemes, is not preserved. These effects are striking and are illustrated in Fig. 12 for w_r with $\alpha = \alpha_3$, $t = 0.7$, and for $N = M = 50$. This figure should be compared with Fig. 11 for $t = 0.7$. The (correct) approach leading to Fig. 11 gives an accurate

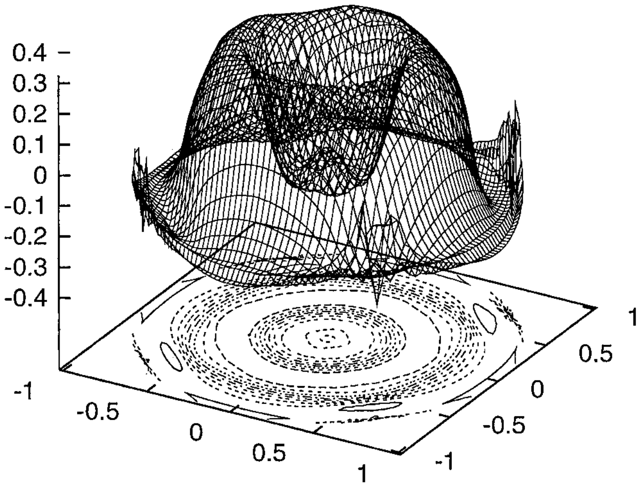

FIG. 12. Graph of the shear strain w_r at the time $t = 0.7$ over the (x, y)-plane for the axisymmetric quasilinear problem ($\alpha = \alpha_3$). This graph is computed in body-fitted coordinates by the faulty alternative formulation with $N = M = 50$. The ineffectiveness of this approach is signaled by the symmetry-destroying oscillations near where the diagonals intersect the circular boundary. The level curves of this graph suggest that axisymmetry is also lost near the center. This figure should be compared with Fig. 11.

description of the boundary behavior and behavior at the origin, preserves the axisymmetry, and exhibits improved accuracy as the grid is refined.

7. COMMENTS

We have formulated a second-order Godunov method that robustly handles shocks, focusing effects, and nonconvex constitutive relations for the nonlinear wave equation governing antiplane motions of incompressible nonlinearly elastic cylinders. Since our class of problems is restricted, we were able to focus our attention on those places where difficulties could be expected, and thus to manage comfortably without using adaptivity such as that developed by [33]. For problems in which there are a wider variety of waves present, it would probably be necessary to replace Davis's Riemann solver with something more sophisticated.

We tempted fate by our choice of body-fitted coordinates in Section 5, which produced serious distortions at the intersections of 45° lines with the bounding circle. Nevertheless, the resulting computations remain accurate provided that we avoid the dangers described in Section 5.6. (To avoid testing body-fitted coordinates under the extreme conditions we imposed on them, we could have broken up the unit disk into five regions, bounded by a square centered at the origin, by rays going outward from the corners of the square, and by the outer circle, and then mapping each of these regularly onto a square, at the cost of matching the computations across common boundaries.)

We carried out other computations for CFL numbers 0.5 and 0.9. The differences in the computations from those shown here for CFL number 0.7 were slight.

The variables in (5.2) should satisfy the compatibility condition $u_y = z_x$. To check whether this condition was conserved, we computed $u_y - z_x$ for our solution with body-fitted coordinates on the time interval [0, 1] for different CFL numbers. Initially the maximum of $|u_y - z_x|$ was high (approximately 5, because of the initial discontinuity) and then diminished until the wave hit the boundary. Here the maximum (approximately 1) was attained near the singularities of the body-fitted coordinates. Although our computational scheme made no provision to conserve $u_y - z_x$, the good agreement between the one-dimensional (axisymmetric) solutions and the two-dimensional solutions indirectly suggest that.

Our methods were inspired in part by those used in gas dynamics. Despite the very different character of the governing equations (ours have a more complicated dependence on the strains and are genuinely not genuinely nonlinear), we succeeded in obtaining very accurate results.

Our results do not indicate any singular behavior associated with focusing at the origin, and do not indicate any instability for soft materials (having sublinear constitutive functions). As we mentioned in the Introduction (Section 1), such effects are exhibited for many other problems of elasticity. We attribute their absence here more to the incompressibility than to the limited repertoire of shearing deformations available in antiplane motions.

We might expect the nonconvexity of the constitutive equations for shear to lead to possible computational complications as they are known to lead to complications in theory (cf. [11]). We have found none for the data we used. We have made no special provisions for treating them, the study of which would not promote our main aim of examining the possibility of singularities as a result of focusing and nonlinear material response. We simply allowed the dissipation inherent in our Godunov scheme to serve as an admissibility criterion. We would expect a far richer repertoire of response when the constraint of antiplanarity is lifted. In particular, the not completely understood phenomenon of overcompressive shocks (with their delicate stability with respect to viscosity) [11, 14] occurs in bidirectional shearing of incompressible elastic media [3, Sec. 16.5].

ACKNOWLEDGMENTS

We thank Harland Glaz and the referees for helpful comments. The research of Lott was supported in part by National Science Foundation Grant DMS 98-03605 and the Foundation at the New Jersey Institute of Technology. The research of Antman was supported in part by National Science Foundation Grant DMS 99 71823 and by ARO-MURI97 Grant No. DAAG55-97-1-0114 to the Center for Dynamics and Control of Smart Structures. The research of Szymczak was supported by the Office of Naval Research, Code 311.

REFERENCES

1. A. S. Almgren, J. B. Bell, and P. Colella, Cartesian grid projection methods for the incompressible Euler equations in complex geometries, *SIAM J. Sci. Comp.* **18**, 1289 (1997).
2. S. S. Antman, Regular and singular problems for large elastic deformations of tubes, wedges, and cylinders, *Arch. Rational Mech. Anal.* **83**, 1 (1983); Corrigenda, ibid. **95**, 391 (1986).
3. S. S. Antman, *Nonlinear Problems of Elasticity* (Springer-Verlag, New York, 1995).
4. S. S. Antman and J. E. Osborn, The principle of virtual work and integral laws of motion, *Arch. Rational Mech. Anal.* **69**, 231 (1979).
5. S. S. Antman and W. G. Szymczak, Nonlinear elastoplastic waves, *Contemp. Math* **100**, 27 (1989).
6. J. M. Ball, Discontinuous equilibrium solutions and cavitation in nonlinear elasticity, *Phil. Trans. Roy. Soc. Lond.* **A306**, 557 (1982).
7. J. B. Bell, P. Colella, and J. A. Trangenstein, Higher-order Godunov methods for general systems of hyperbolic conservation laws, *J. Comput. phys.* **82**, 362 (1989).
8. J. B. Bell, J. M. Solomon, and W. G. Szymczak, Projection methods for viscous incompressible flow on quadrilateral grids, *AAIA Journal* **32**, 1961 (1994).
9. M. J. Berger and R. J. Leveque, Adaptive mesh refinement using wave-propagation algorithms for hyperbolic systems, *SIAM J. Numer. Anal.* **35**, 2298 (1998).
10. G. Chesshire and W. D. Henshaw, A scheme for conservative interpolation on overlapping grids, *SIAM J. Sci. Comput.* **15**, 819 (1994).
11. C. M. Dafermos, *Hyperbolic Conservation Laws in Continuum Physic.* (Springer-Verlags, New York, 2000).
12. S. F. Davis, Simplified second-order Godunov-type methods, *SIAM J. Sci. Stat. Comput.* **9**, 445 (1988).
13. B. Engquist and S. Osher, One-sided difference approximations for nonlinear conservation laws, *Math. of Comp.* **36**, 321 (1981).
14. H. Freistühler, Instability of vanishing viscosity approximation to hyperbolic systems of conservation laws with rotational invariance, *J. Diff. Eqs.* **87**, 205 (1990).
15. X. Garaizar, Solution of a Riemann problem for elasticity, *J. Elasticity* **26**, 43 (1991).
16. X. Garaizar and J. A. Trangenstein, Adaptive mesh refinement and front-tracking for shear bands in an antiplane shear model, *SIAM J. Sci. Comput.* **20**, 750 (1998).
17. P. Glaister, An algorithm for the shallow water equations with body fitted meshes, *Comp. Mech.* **8**, 313 (1991).
18. A. Gray and M. A. Pinsky, Computer graphics and a new Gibbs phenomenon for Fourier-Bessel series, *Experimental Math.* **1**, 313 (1992).
19. J. K. Knowles, On finite anti-plane shear for incompressible elastic materials, *J. Austral. Math. Soc. Ser. B* **19**, 400 (1976).
20. P. Knupp and S. Steinberg, *Foundations of Grid Generation* (CRC Press, Boca Raton, Florida, 1993).

21. P. D. Lax, *Hyperbolic Systems of Conservation Laws and the Mathematical Theory of Shock Waves* (Soc. Industr. & Appl. Math, Philadelphia, 1973).
22. T.-P. Liu, The Riemann problem for general systems of conservation laws, *J. Diff. Eqs.* **18**, 219 (1975).
23. R. B. Pember, J. B. Bell, P. Colella, W. Y. Crutchfield, and M. L. Welcome, An adaptive Cartesian grid method for unsteady compressible flow in irregular regions, *J. Comput. Phys.* **120**, 278 (1995).
24. R. B. Pember, J. A. Greenough, and P. Colella, An adaptive, higher-order Godunov method for gas dynamics in three-dimensional orthogonal curvilinear coordinates, Technical Report UCRL-JC-123244 (Lawrence Livermore National Laboratory, 1996).
25. T. H. Pulliam and J. L. Steger, Implicit finite-difference simulations of three-dimensional compressible flow, *AIAA J.* **18**, 159 (1980).
26. C. W. Schulz-Rinne, J. P. Collins, and H. M. Glaz, Numerical solution of the Riemann problem for two-dimensional gas dynamics, *SIAM J. Sci. Comput.* **14**, 1394 (1993).
27. K. A. Pericak-Spector and S. J. Spector, Nonuniqueness for a hyperbolic system: Cavitation in nonlinear elastodynamics, *Arch. Rational Mech. Anal.* **101**, 293 (1988).
28. K. A. Pericak-Spector and S. J. Spector, Dynamic cavitation with shocks in nonlinear elasticity, *Proc. Roy. Soc. Edinburgh* **A127**, 837 (1997).
29. R. T. Shield and A. E. Green, On certain methods in the stability theory of continuous systems, *Arch. Rational. Mech. Anal.* **12**, 354 (1963).
30. Z. Tang and T. C. T. Ting, Wave curves for the Riemann problem of plane waves in isotropic elastic solids, *Int. J. Eng. Sci.* **25**, 1343 (1987).
31. P. D. Thomas and C. K. Lombard, Geometric conservation law and its application to flow computations on moving grids, *AIAA J.* **17**, 1030 (1979).
32. J. A. Trangenstein, A second-order Godunov algorithm for two-dimensional solid mechanics, *Comp. Mech.* **13**, 343 (1994).
33. J. A. Trangenstein, Adaptive mesh refinement for wave propagation in nonlinear solids, *SIAM J. Sci. Comp.* **16**, 819 (1995).
34. J. A. Trangenstein and P. Colella, A higher-order Godunov method for modeling finite deformation in elastic-plastic solids, *Comm. Pure Appl. Math.* **44**, 41 (1991).
35. J. A. Trangenstein and R. B. Pember, The Riemann problem for longitudinal motion in an elastic-plastic bar, *SIAM J. Sci. Stat. Comput.* **12**, 180 (1991).
36. P. Vijayan and Y. Kallinderis, A 3D finite-volume scheme for the Euler equations on adaptive tetrahedral grids, *J. Comput. Phys.* **113**, 249 (1994).
37. B. Wendroff, The Riemann problem for materials with nonconvex equations of state, II: General flow, *J. Math. Anal. Appl.* **38**, 640 (1972).
38. P. Woodward and P. Colella, The numerical simulation of two-dimensional fluid flow with strong shocks, *J. Comput. Phys.* **54**, 115 (1984).